

# *In vivo* investigation of temporal effects and drug delivery induced by transdermal microneedles with optical coherence tomography

Meng-Tsan Tsai,<sup>1,2</sup> I-Chi Lee,<sup>3,\*</sup> Zhung-Fu Lee,<sup>1</sup> Hao-Li Liu,<sup>1,2</sup> Chun-Chieh Wang,<sup>2,4,5</sup> Yo-Chun Choia,<sup>1</sup> Hsin-Yi Chou,<sup>1</sup> and Jiann-Der Lee<sup>1,6</sup>

<sup>1</sup>Department of Electrical Engineering, Chang Gung University, Taoyuan, 33302, Taiwan

<sup>2</sup>Medical Imaging Research Center, Institute for Radiological Research, Chang Gung University and Chang Gung Memorial Hospital at Linkou, Taoyuan, Taiwan

<sup>3</sup>Graduate Institute of Biochemical and Biomedical Engineering, Chang Gung University, Taoyuan, Taiwan

<sup>4</sup>Departments of Radiation Oncology, Chang Gung Memorial Hospital, Linkou, Taiwan

<sup>5</sup>Department of Medical Imaging and Radiological Science, Chang Gung University, Taoyuan, Taiwan

<sup>6</sup>jdlee@mail.cgu.edu.tw

<sup>\*</sup>iclee@mail.cgu.edu.tw

**Abstract:** Transdermal drug-delivery systems (TDDS) have been a growing field in drug delivery because of their advantages over parenteral and oral administration. Recent studies illustrate that microneedles (MNs) can effectively penetrate through the stratum corneum barrier to facilitate drug delivery. However, the temporal effects on skin and drug diffusion are difficult to investigate *in vivo*. In this study, we used optical coherence tomography (OCT) to observe the process by which MNs dissolve and to investigate the temporal effects on mouse skin induced by MNs, including the morphological and vascular changes. Moreover, the recovery process of the skin was observed with OCT. Additionally, we proposed a method to observe drug delivery by estimation of cross-correlation relationship between sequential 2D OCT images obtained at the same location, reflecting the variation in the backscattered intensity due to the diffusion of the rhodamine molecules encapsulated in MNs. Our observations supported the hypothesis that the temporal effects on skin due to MNs, the dissolution of MNs, and the drug diffusion process can be quantitatively evaluated with OCT. The results showed that OCT can be a potential tool for *in vivo* monitoring of effects and outcomes when MNs are used as a TDDS.

©2016 Optical Society of America

**OCIS codes:** (110.4500) Optical coherence tomography; (170.2655) Functional monitoring and imaging; (170.3880) Medical and biological imaging.

## References and links

1. L. L. Brunton, B. Chabner, and B. Knollman, *Goodman & Gilman's the Pharmacological Basis of Therapeutics* (McGraw-Hill Medical New York, 2011) vol. 12, pp. 17–41.
2. R. B. Berkowitz, D. I. Bernstein, C. LaForce, A. J. Pedinoff, A. R. Rooklin, C. R. Damaraju, B. Mesarina-Wicki, and K. B. Nolop, "Onset of action of mometasone furoate nasal spray (NASONEX) in seasonal allergic rhinitis," *Allergy* **54**(1), 64–69 (1999).
3. J. Yu and Y. W. Chien, "Pulmonary drug delivery: physiologic and mechanistic aspects," *Crit. Rev. Ther. Drug Carrier Syst.* **14**(4), 395–453 (1997).
4. B. F. Choonara, Y. E. Choonara, P. Kumar, D. Bijukumar, L. C. du Toit, and V. Pillay, "A review of advanced oral drug delivery technologies facilitating the protection and absorption of protein and peptide molecules," *Biotechnol. Adv.* **32**(7), 1269–1282 (2014).
5. S. P. Sullivan, D. G. Koutsonanos, M. Del Pilar Martin, J. W. Lee, V. Zarnitsyn, S. O. Choi, N. Murthy, R. W. Compans, I. Skountzou, and M. R. Prausnitz, "Dissolving polymer microneedle patches for influenza vaccination," *Nat. Med.* **16**(8), 915–920 (2010).
6. K. van der Maaden, W. Jiskoot, and J. Bouwstra, "Microneedle technologies for (trans)dermal drug and vaccine delivery," *J. Control. Release* **161**(2), 645–655 (2012).
7. S. Indermun, R. Luttge, Y. E. Choonara, P. Kumar, L. C. du Toit, G. Modi, and V. Pillay, "Current advances in the fabrication of microneedles for transdermal delivery," *J. Control. Release* **185**, 130–138 (2014).

8. J. B. Carey, A. Vrdoljak, C. O'Mahony, A. V. Hill, S. J. Draper, and A. C. Moore, "Microneedle-mediated immunization of an adenovirus-based malaria vaccine enhances antigen-specific antibody immunity and reduces anti-vector responses compared to the intradermal route," *Sci. Rep.* **4**, 6154 (2014).
9. M. R. Prausnitz, "Microneedles for transdermal drug delivery," *Adv. Drug Deliv. Rev.* **56**(5), 581–587 (2004).
10. J. Enfield, M.-L. O'Connell, K. Lawlor, E. Jonathan, C. O'Mahony, and M. Leahy, "In-vivo dynamic characterization of microneedle skin penetration using optical coherence tomography," *J. Biomed. Opt.* **15**(4), 046001 (2010).
11. R. F. Donnelly, D. I. Morrow, T. R. Singh, K. Migalska, P. A. McCarron, C. O'Mahony, and A. D. Woolfson, "Processing difficulties and instability of carbohydrate microneedle arrays," *Drug Dev. Ind. Pharm.* **35**(10), 1242–1254 (2009).
12. S. F. Lahiji, M. Dangol, and H. Jung, "A patchless dissolving microneedle delivery system enabling rapid and efficient transdermal drug delivery," *Sci. Rep.* **5**, 7914 (2015).
13. I. C. Lee, J. S. He, M. T. Tsai, and K. C. Lin, "Fabrication of a novel partially dissolving polymer microneedle patch for transdermal drug delivery," *J. Mater. Chem. B Mater. Biol. Med.* **3**(2), 276–285 (2015).
14. T. Rattanapak, J. Birchall, K. Young, M. Ishii, I. Meglinski, T. Rades, and S. Hook, "Transcutaneous immunization using microneedles and cubosomes: mechanistic investigations using Optical Coherence Tomography and Two-Photon Microscopy," *J. Control. Release* **172**(3), 894–903 (2013).
15. R. F. Donnelly, M. J. Garland, D. I. Morrow, K. Migalska, T. R. Singh, R. Majithiya, and A. D. Woolfson, "Optical coherence tomography is a valuable tool in the study of the effects of microneedle geometry on skin penetration characteristics and in-skin dissolution," *J. Control. Release* **147**(3), 333–341 (2010).
16. S. Y. Yang, E. D. O'Ceirbhail, G. C. Sisk, K. M. Park, W. K. Cho, M. Villiger, B. E. Bouma, B. Pomahac, and J. M. Karp, "A bio-inspired swellable microneedle adhesive for mechanical interlocking with tissue," *Nat. Commun.* **4**, 1702 (2013).
17. D. Huang, E. A. Swanson, C. P. Lin, J. S. Schuman, W. G. Stinson, W. Chang, M. R. Hee, T. Flotte, K. Gregory, C. A. Puliafito, and et, "Optical coherence tomography," *Science* **254**(5035), 1178–1181 (1991).
18. D. C. Adler, Y. Chen, R. Huber, J. Schmitt, J. Connolly, and J. G. Fujimoto, "Three-dimensional endomicroscopy using optical coherence tomography," *Nat. Photonics* **1**(12), 709–716 (2007).
19. L. An, P. Li, T. T. Shen, and R. Wang, "High speed spectral domain optical coherence tomography for retinal imaging at 500,000 A-lines per second," *Biomed. Opt. Express* **2**(10), 2770–2783 (2011).
20. J. Xi, A. Zhang, Z. Liu, W. Liang, L. Y. Lin, S. Yu, and X. Li, "Diffraction catheter for ultrahigh-resolution spectral-domain volumetric OCT imaging," *Opt. Lett.* **39**(7), 2016–2019 (2014).
21. I. Grulkowski, J. J. Liu, B. Potsaid, V. Jayaraman, J. Jiang, J. G. Fujimoto, and A. E. Cable, "High-precision, high-accuracy ultralong-range swept-source optical coherence tomography using vertical cavity surface emitting laser light source," *Opt. Lett.* **38**(5), 673–675 (2013).
22. D. Nankivil, A. H. Dhalla, N. Gahm, K. Shia, S. Farsi, and J. A. Izatt, "Coherence revival multiplexed, buffered swept source optical coherence tomography: 400 kHz imaging with a 100 kHz source," *Opt. Lett.* **39**(13), 3740–3743 (2014).
23. C. H. Yang, M. T. Tsai, S. C. Shen, C. Y. Ng, and S. M. Jung, "Feasibility of ablative fractional laser-assisted drug delivery with optical coherence tomography," *Biomed. Opt. Express* **5**(11), 3949–3959 (2014).
24. S. Yousefi, J. Qin, and R. K. Wang, "Super-resolution spectral estimation of optical micro-angiography for quantifying blood flow within microcirculatory tissue beds in vivo," *Biomed. Opt. Express* **4**(7), 1214–1228 (2013).
25. W. J. Choi, Z. Zhi, and R. K. Wang, "In vivo OCT microangiography of rodent iris," *Opt. Lett.* **39**(8), 2455–2458 (2014).
26. P. Zhang, K. Mehta, S. Rehman, and N. Chen, "Imaging single chiral nanoparticles in turbid media using circular-polarization optical coherence microscopy," *Sci. Rep.* **4**, 4979 (2014).
27. Y.-J. Hong, S. Makita, S. Sugiyama, and Y. Yasuno, "Optically buffered Jones-matrix-based multifunctional optical coherence tomography with polarization mode dispersion correction," *Biomed. Opt. Express* **6**(1), 225–243 (2015).
28. S. Wang, A. L. Lopez 3rd, Y. Morikawa, G. Tao, J. Li, I. V. Larina, J. F. Martin, and K. V. Larin, "Noncontact quantitative biomechanical characterization of cardiac muscle using shear wave imaging optical coherence tomography," *Biomed. Opt. Express* **5**(7), 1980–1992 (2014).
29. K. M. Kennedy, L. Chin, R. A. McLaughlin, B. Latham, C. M. Saunders, D. D. Sampson, and B. F. Kennedy, "Quantitative micro-elastography: imaging of tissue elasticity using compression optical coherence elastography," *Sci. Rep.* **5**, 15538 (2015).
30. E. Sattler, R. Kästle, and J. Welzel, "Optical coherence tomography in dermatology," *J. Biomed. Opt.* **18**(6), 061224 (2013).
31. B. Kim, S. H. Lee, C. J. Yoon, Y. S. Gho, G.-O. Ahn, and K. H. Kim, "In vivo visualization of skin inflammation by optical coherence tomography and two-photon microscopy," *Biomed. Opt. Express* **6**(7), 2512–2521 (2015).
32. S. M. Srinivas, J. F. de Boer, H. Park, K. Keikhanzadeh, H. E. Huang, J. Zhang, W. Q. Jung, Z. Chen, and J. S. Nelson, "Determination of burn depth by polarization-sensitive optical coherence tomography," *J. Biomed. Opt.* **9**(1), 207–212 (2004).
33. M. G. Ghosn, V. V. Tuchin, and K. V. Larin, "Nondestructive quantification of analyte diffusion in cornea and sclera using optical coherence tomography," *Invest. Ophthalmol. Vis. Sci.* **48**(6), 2726–2733 (2007).
34. M. G. Ghosn, N. Sudheendran, M. Wendt, A. Glasser, V. V. Tuchin, and K. V. Larin, "Monitoring of glucose permeability in monkey skin in vivo using optical coherence tomography," *J. Biophotonics* **3**(1-2), 25–33 (2010).

35. M. T. Tsai, C. K. Lee, K. M. Lin, Y. X. Lin, T. H. Lin, T. C. Chang, J. D. Lee, and H. L. Liu, "Quantitative observation of focused-ultrasound-induced vascular leakage and deformation via fluorescein angiography and optical coherence tomography," *J. Biomed. Opt.* **18**, 101307 (2013).
36. A. Mariampillai, B. A. Standish, E. H. Moriyama, M. Khurana, N. R. Munce, M. K. Leung, J. Jiang, A. Cable, B. C. Wilson, I. A. Vitkin, and V. X. Yang, "Speckle variance detection of microvasculature using swept-source optical coherence tomography," *Opt. Lett.* **33**(13), 1530–1532 (2008).
37. D. W. Cadotte, A. Mariampillai, A. Cadotte, K. K. Lee, T.-R. Kiehl, B. C. Wilson, M. G. Fehlings, and V. X. Yang, "Speckle variance optical coherence tomography of the rodent spinal cord: in vivo feasibility," *Biomed. Opt. Express* **3**(5), 911–919 (2012).
38. A. Roggan, M. Friebel, K. Dörschel, A. Hahn, and G. Müller, "Optical properties of circulating human blood in the wavelength range 400–2500 nm," *J. Biomed. Opt.* **4**(1), 36–46 (1999).
39. N. Bosschaart, G. J. Edelman, M. C. G. Aalders, T. G. van Leeuwen, and D. J. Faber, "A literature review and novel theoretical approach on the optical properties of whole blood," *Lasers Med. Sci.* **29**(2), 453–479 (2014).

## 1. Introduction

For many years, drugs have been used to treat diseases and to improve health, and the development of drug-delivery systems for active pharmaceutical ingredients is an important task. The most common administration routes include oral, parenteral and transdermal routes [1]. Some less explored routes, such as nasal and pulmonary delivery, can be utilized for specific medical purposes [2,3]. However, each administration route has specific benefits and drawbacks. Parenteral administration can provide the advantages of quick onset and high bioavailability; however, the disadvantages of injection-induced pain and safety concerns limit patient compliance. In addition, oral drug-delivery systems offer the advantages of convenient administration, a large surface area with rich blood supply for absorption, and low cost. Nevertheless, limitations in drug degradation in first-pass metabolism, poor absorption, local irritation and low bioavailability are seen [4].

Microneedles (MNs) have recently been developed as an alternative drug-delivery system that minimizes the abovementioned disadvantages [5–8]. As a transdermal drug-delivery system, MN arrays improve drug delivery whereby the microscopic needles transiently pierce through stratum corneum, inducing the micro-channel array to enable drug delivery to deeper tissue. MNs (50–900  $\mu\text{m}$  in height, up to 200 MNs/cm<sup>2</sup>) in diverse geometries can be produced from silicon, metal, carbohydrates and polymers using various microfabrication techniques [9–12]. The length of MNs must be long enough to penetrate the dermis but short enough to avoid harming dermal nerves. Compared to metallic MNs, biodegradable MNs could be a promising approach to deliver drugs due to less biohazardous sharp waste and a higher efficiency of drug delivery.

When MNs are used for transdermal drug delivery, it is very important that appropriate monitoring techniques are needed to determine the penetration depth and the efficiency of drug delivery, enabling the performance of MNs to be evaluated. However, because the penetration depth of MNs can reach several hundred micrometers in the skin, *in vivo* investigation of effects on the skin is also difficult. Currently, several approaches have been proposed to monitor the effects on the skin induced by MNs, including confocal microscopy [13], two-photon microscopy [14], and optical coherence tomography (OCT) [15,16]. For confocal microscopy, the imaging depth is limited to a depth range of less than 300  $\mu\text{m}$ , which is not deep enough to observe the induced effects in the deeper layer. In addition, a fluorescent dye must be added to the MNs when confocal or two-photon microscopy is used. By contrast, OCT is based on an interferometer configuration and the microstructure of the sample can be reconstructed by receiving the interference signal induced by the backscattered light from the sample and the reference arms [17,18]. However, due to the scattering and absorption properties of the biological tissue, the OCT imaging depth is limited to be approximately 2–3 mm. Additionally, based on spectral-domain OCT (SD-OCT) [19,20] or swept-source OCT (SS-OCT) [21–23] mechanism, the imaging speed and the system sensitivity can achieve hundreds frames/s and more than 100 dB, respectively. Moreover, functional information of the biological tissue such as angiography [24,25], birefringence [26,27], and elasticity [28,29] can be obtained with OCT scanning without extraneous agents. Many groups have demonstrated that OCT could be a powerful tool for various dermatology

applications including skin cancer [30], skin diseases [31], and burn damage [32]. However, few OCT studies have focused on drug delivery. In our previous report, the variation of OCT intensity due to liquid diffusion through the laser-induced microscopic ablation zones on the fingernail can be observed by the estimation of speckle variance. However, such method is difficult to be applied to dynamically observe the drug delivery from the MN into the surrounding tissue [23]. Additionally, Ghosn et al. proposed that the estimation of the slope of the OCT depth profile can be utilized to monitor glucose permeability in the monkey skin and the cornea [33,34]. However, the method only presented the averaged results, but no depth information of drug diffusion can be acquired.

In this study, we use OCT to investigate the temporal effects on skin induced by MNs during transdermal drug delivery. OCT is implemented for *in vivo* observation of the dissolution process of MNs in mouse skin, which enables to evaluate the dissolving ability of MNs in skin. The morphological changes with time due to MNs are also investigated. Moreover, OCT is used to reconstruct the micro-angiography of mouse skin and to observe the changes in micro-angiography with time due to the insertion of MNs, enabling the dynamic evaluation of skin damage and recovery. Finally, a method is proposed to evaluate the drug diffusion in mouse skin, according to the estimation of cross-correlation coefficients between time-series OCT images obtained at the same skin location.

## 2. Experimental methods and system

### 2.1 Experimental methods and MNs

In this study, mice (C57 wild-type, male, 7–8 weeks old) were chosen and anesthetized with a mixed aesthetic composed of oxygen and phenobarbital. To reduce motion artefacts during OCT scanning, the mice were held on a customized mount. The animal testing in this study was approved by the Laboratory Animal Center, Chang Gung University (IACUC Approval No: CGU13-126). The methods were carried out in accordance with the approved guidelines. For manufacture of the MN patches, a partially dissolving polymeric MN patch was prepared by using Polyvinyl alcohol (PVA): polyvinylpyrrolidone (PVP) = 1:4 as previously described [13]. The dimensions of the MNs on the array were a mean height of 630  $\mu\text{m}$  with 351 pyramidal needles in a  $6 \times 13$  mm area. Our previous study revealed that the height loss of PVA: PVP = 1:4 MNs was less than 5%. To assess the feasibility of using OCT for the observation of drug diffusion following transdermal delivery, rhodamine 6G was encapsulated within the MNs.

### 2.2 OCT system

For this study, an SS-OCT system at 1060 nm was implemented for mouse skin scanning. The system setup is shown in Fig. 1. The scanning rate of swept-source is 100 kHz (SSOCT-1060, AXSUN Technologies Inc., MA, USA) with a scanning bandwidth of 100 nm, which can provide an output power of 15 mW. Then, a light source was connected to a Michelson interferometer, and the light was split into the reference and sample arms. The reflected or backscattered light from the reference and sample arms was split again by the other fiber coupler with a coupling coefficient of 50/50. In the sample arm, a dual-axis scanner (GVS302, Thorlabs Inc., NJ, USA) was used to provide lateral and transverse scanning, and then, the optical beam from the scanner was incident on a scan lens (LSM02-BB, Thorlabs Inc., NJ, USA). To compensate the dispersion resulting from the scan lens, a dispersion compensator was inserted in the reference arm. The two output ends of the second coupler were connected to a balanced detector (PDB460C, Thorlabs Inc., NJ, USA). For data acquisition and resampling, a high-speed digitizer (ATS-9350, Alazar Technologies Inc., QC, Canada) was implemented with a sampling rate of 500 MHz. The axial and transverse resolutions of the OCT system are approximately 6 and 7  $\mu\text{m}$ , respectively. The system sensitivity was measured to be 101 dB at a depth of 1mm. For vascular imaging based on OCT images, two B-mode scans at the same location were recorded and the SV between the two sequential B-mode scans was estimated. Furthermore, to perform 3D imaging, 500 B-mode locations were

scanned. Therefore, a 3D OCT volume consists of 1000 B-modes scans, enabling a 3D vascular image to be acquired. The physical scanning range of the OCT system is 3 mm × 3 mm × 2 mm.

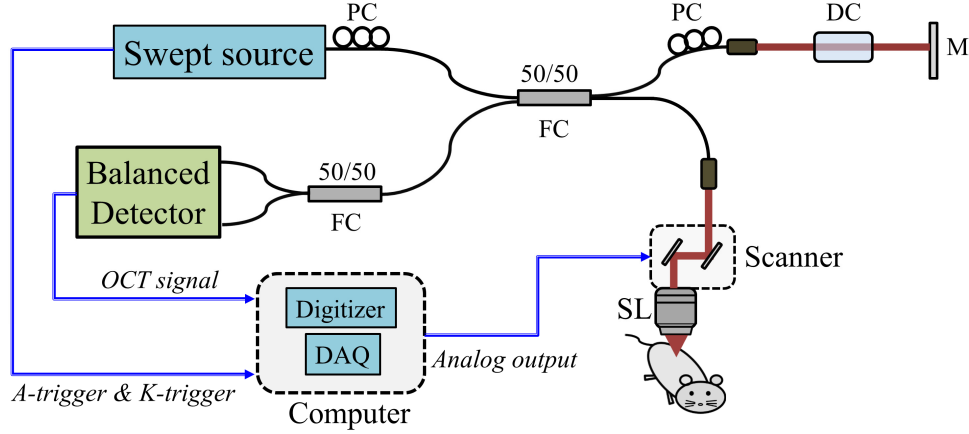


Fig. 1. Schematic of the 1060-nm SS-OCT system. PC: polarization controller; FC: fiber coupler; DC: dispersion compensation; M: mirror; SL: scanning lens.

In this study, vascular images from OCT images were acquired by estimating the SV of sequential B-mode scans obtained at the same location, expressed as

$$SV_{ijk} = \frac{1}{N} \sum_{k=1}^N (I_{ijk} - \frac{1}{N} \sum_{k=1}^N I_{ijk})^2 \quad (1)$$

where  $N$  and  $k$  are the frame number and the  $k$ th frame for the SV estimation [32].  $i$  and  $j$  represent the pixels along the axial and transverse directions, respectively. Here, the moving particles in the tissue, such as red blood cells, result in time-dependent intensity variance between sequential B-mode scans obtained at the same location; in contrast, the static particles in tissue correspond to low intensity variation between sequential B-mode scans. Therefore, the static tissue and the region of red blood cells can be differentiated from the estimation of the SV.

In addition, to observe drug or particle diffusion into skin, a method based on the evaluation of cross-correlation relationship from OCT B-mode scans was proposed. The estimation of the cross-correlation coefficient,  $C(x,z)$ , can be written as

$$C(x,z) = \sum_{i=1}^n \sum_{j=1}^m \frac{[I_A(x+i,z+j) - \bar{I}_A][I_B(x+i,z+j) - \bar{I}_B]}{\sqrt{[I_A(x+i,z+j) - \bar{I}_A]^2 [I_B(x+i,z+j) - \bar{I}_B]^2}} \quad (2)$$

where  $n$  and  $m$  are the grid sizes. Here, both  $n$  and  $m$  equal 5.  $I_A(x,z)$  and  $I_B(x,z)$  indicate the OCT intensities of the two images. Then,  $\bar{I}_A$  and  $\bar{I}_B$  are the mean values of each grid.  $x$  and  $z$  represent the locations along the transverse and depth directions, respectively. To observe the drug diffusion process, time-series B-mode scans were recorded and the B-mode scan in the beginning of insertion of MN patch was chosen as the reference image. Then, the correlation coefficients were estimated between the reference image and each time-series B-mode scan, according to Eq. (2). In this study,  $N$  is equal to 2. In the previous reports, estimation of correlation coefficients between OCT images could be applied to acquire vascular images. To remove the low-correlation contribution from the vessels, the same mouse skin location was continuously scanned by OCT before the MN insertion. Then, two sequential B-scans before the MN insertion were used to estimate the correlation coefficients. According to the estimated result, most of contribution from the vessels can be removed when a threshold value

was set to be 0.15 in our system. Moreover, the value of 0.15 can also effectively remove the contribution from static tissues. Then, to observe the drug diffusion process, the same skin location was repeatedly scanned with OCT after the MN insertion. The B-mode scan in the beginning of the MN insertion was used as the reference image and then, the correlation coefficients were estimated between the reference image and each time-series B-mode scan. Here, the value of 0.15 might be changed when using different OCT systems and scanning the different tissue locations. However, the threshold value can be determined according to the aforementioned procedure. In our OCT system, a threshold value of 0.15 was set to reject the vascular contribution.

### 3. Results

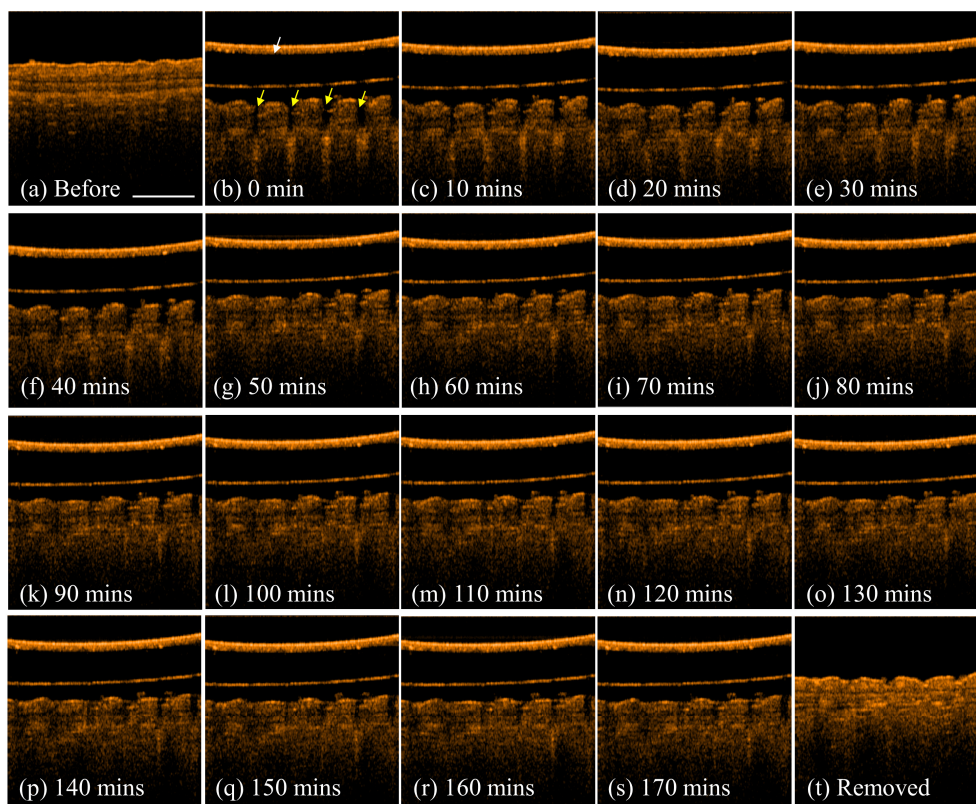


Fig. 2. 2D OCT images of the same skin location on the mouse ear obtained (a) before inserting the microneedle patch on the skin and (b) 0 min, (c) 10 mins, (d) 20 mins, (e) 30 mins, (f) 40 mins, (g) 50 mins, (h) 60 mins, (i) 70 mins, (j) 80 mins, (k) 90 mins, (l) 100 mins, (m) 110 mins, (n) 120 mins, (o) 130 mins, (p) 140 mins, (q) 150 mins, (r) 160 mins, (s) 170 mins, and (t) after removing the MN patch. The scale bar in (a) represents 1 mm in length.

To *in vivo* observe the dissolution process of polymer MNs in mouse skin, OCT was used to record time-series 2D images before and after the insertion of a MN patch on the ear skin of a mouse. Figure 2 shows the time-series OCT images of the mouse skin obtained (a) before the insertion of MN patch, (b)-(s) after the insertion at varying time points (0, 10, 20, 30, 40, 50, 60, 70, 80, 90, 100, 110, 120, 130, 140, 150, 160, and 170 mins), and (t) after removing the patch. From Fig. 2(a), the intact skin morphology without the MN insertion can be observed. After the insertion of the MN patch, the MNs penetrated into the skin and induced the micro-channel array in the skin as indicated by the yellow arrows in Fig. 2(b). The white arrow in Fig. 2(b) represents the patch structure. Moreover, it can be found that the diameters and the penetration depths of micro-channels gradually became smaller with time as a result of the

MN dissolution. Then, after removing the MN patch, the skin shrank and the induced micro-channels disappeared. However, compared with Fig. 2(a), indentations on the skin surface can be seen after removing the MN patch, as shown in Fig. 2(t).

To further quantitatively evaluate the dissolution process of the MNs in mouse skin, the same experimental procedure in Fig. 2 was repeated. To *in vivo* observe the dissolution process of MNs in skin, the mouse ear was fixed on a specially designed mount and scanned with OCT for 180 mins. During OCT measurement, the mouse were anesthetized with a mixed aesthetic composed of oxygen and phenobarbital. With this procedure, the mouse can be stably fixed for a couple of hours. The MN patch was inserted into the ear skin of the mouse, and the skin was scanned by the OCT system to acquire time-series 3D OCT images for 180 mins. After the insertion for 180 mins, the MN patch was removed from the skin. Figure 3 shows the time-series *en-face* OCT images at different depths (100, 200, and 300  $\mu\text{m}$ ), which were extracted from the time-series 3D OCT images. In Fig. 3, the black holes corresponded to the areas of the MNs at the specific depths. To evaluate the time-dependent changes in the areas of the MNs at the different depths, an algorithm was developed to estimate the areas of black holes, which is similar to the algorithm proposed in our previous study [35]. Therefore, the changes in the areas of MNs at the specific depths can be estimated from Fig. 3, as shown in Fig. 4. Figure 4 shows the estimated areas of the MNs at three different depths of 100, 200, and 300  $\mu\text{m}$  as a function of time. The results showed that the area at the specific depth decreased as time increased, resulting from the dissolution of the MNs. Here, the results also showed larger standard deviations in the estimated MN areas, probably resulting from the causes such as different incident angles to the skin surface for each MN, nonuniform distribution of pressure on the patch to insert MNs into skin, and inhomogeneous skin structure. However, the results showed that using OCT enables quantitative evaluation of the dissolution process of MNs in skin.

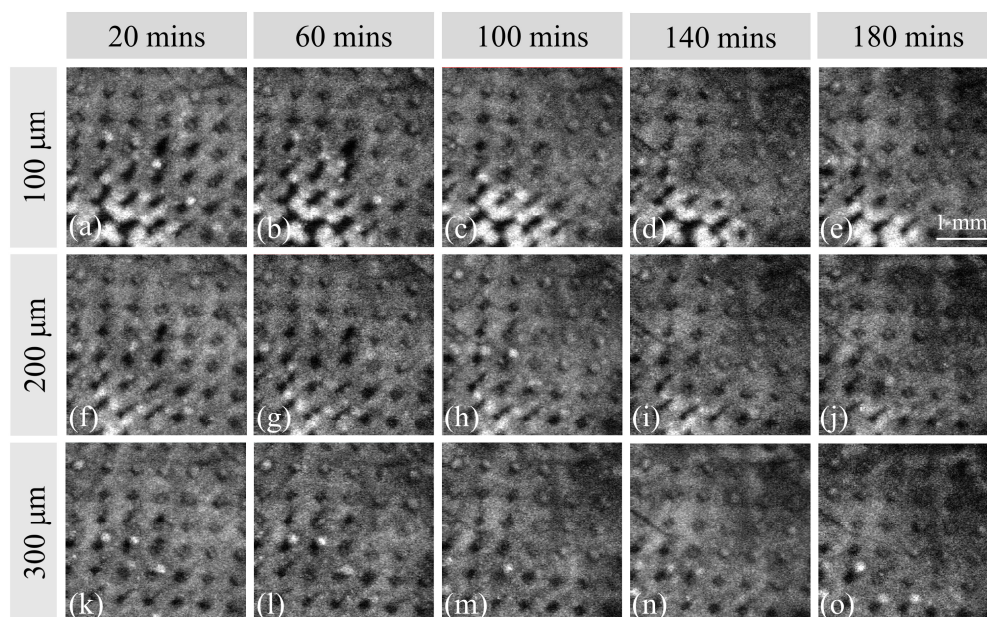


Fig. 3. Time-series *en-face* images at three different depths in the mouse ear skin obtained after the insertion of MN patch for (a), (f), (k) 20 mins; (b), (g), (l) 60 mins; (c), (h), (m) 100 mins; (d), (i), (n) 140 mins; and (e), (j), (o) 180 mins

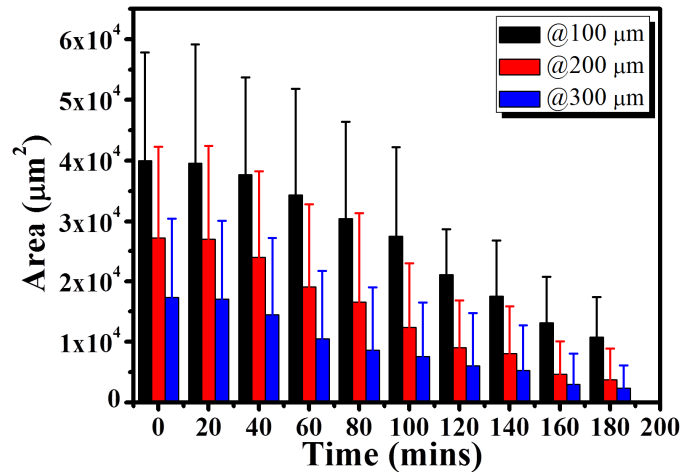


Fig. 4. Estimated areas of MNs at three different depths of 100, 200, and 300  $\mu\text{m}$  as a function of time.

Moreover, to understand the morphological change after removing the MN patch and skin recovery, an MN patch was inserted into the ear skin of another mouse and removed after 180 mins. Before and after removal of the patch at varying time points, the ear skin was scanned with the OCT system to acquire time-series 3D images. To repeatedly scan the same skin area at the different time points, we chose an intersection of two vessels as the marked point, which can be identified by the naked eyes. Before each OCT measurement, both axes of the scanner were driven with constant DC voltages and then, we moved the mouse mount, which was fixed on an accurate translation stage, until the optical beam was exactly incident on the marked point. Therefore, we can make sure that the same region can be repeatedly scanned at the different time points. Figure 5 shows the projection view of the skin surface obtained (a) before the insertion of the MN patch and after removing the MN patch for (b) 0, (c) 12, (d) 24, (e) 36, and (f) 48 hrs. Figures 5(g)-5(l) show the representative B-mode scans obtained at the locations indicated by the red lines in Figs. 5(a)-5(f). Figure 5(a) shows an intact skin surface, and a smooth surface curvature can be identified. However, after removing the MNs, the indentations can be found as indicated by the yellow and red arrows in the projection-view and 2D images, respectively. After 24 hrs, most of the indentations on the skin surface disappeared and after 48 hrs, no indentation on the skin surface were found, illustrating that indentation induced by MN can recover in 48 hrs.

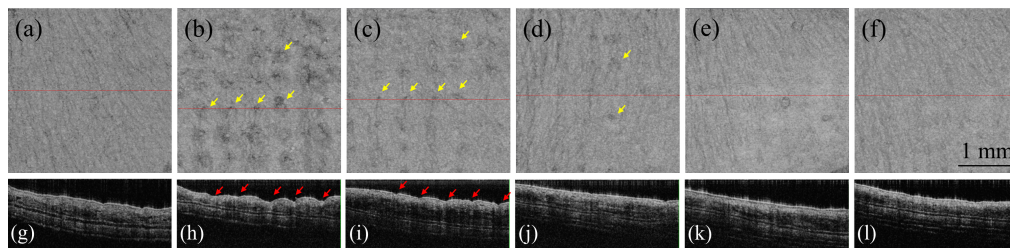


Fig. 5. Projection view of the skin surface obtained (a) before insertion of the MN patch and (b) 0 hr, (c) 12 hrs, (d) 24 hrs, (e) 36 hrs, and (f) 48 hrs after removing the MN patch. (g)-(l): representative B-mode scans corresponding to the locations indicated by the red lines in (a)-(f), respectively.

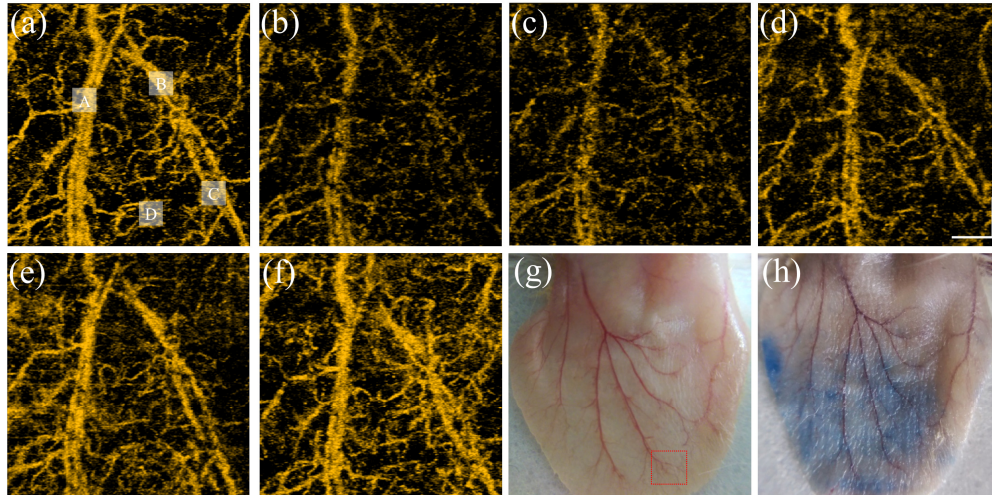


Fig. 6. (a)-(f) Full depth range projection view of OCT angiography obtained (a) before insertion of the MN patch and (b) 0 hr, (c) 12 hrs, (d) 24 hrs, (e) 36 hrs, and (f) 48 hrs after removing the MN patch. (g) A photo of a mouse ear before insertion of a MN patch, and (h) a photo of a mouse ear after removing the MN patch by using Evans blue as a contrast agent for identification of blood leakage. The scale bars in (d) represent 0.5 mm in length.

Although the skin indentations induced by MNs can recover in 48 hrs, the mean height of the MNs used in this study is approximately  $630\ \mu\text{m}$ , which possibly penetrates into the dermal layer and damages the vessels. Therefore, to further understand the effects on vessels due to MNs, OCT images of Fig. 5 were used to estimate speckle variance (SV) between sequential OCT images obtained at the same skin locations to acquire the angiography of skin [36,37]. Here, the moving particles, such as the moving blood cells in vessels, result in larger variations in backscattered intensities between two sequential OCT images captured at the same location. In contrast, the static particles or static tissue structures cause lower intensity variations between sequential OCT images obtained at the same location. Therefore, vessels can be visualized by extracting the regions with higher SV values. Figure 6 shows the projection-view OCT angiographies obtained (a) before the insertion of the MN patch and after removing the MN patch for (b) 0, (c) 12, (d) 24, (e) 36, and (f) 48 hrs. Before the insertion of the MN patch, the vascular pattern was intact and some vessels were broken after removing the MN patch. For red blood cells, the scattering property is much stronger as compared to the absorption property in the 1060-nm spectral range [38,39]. The leaked red blood cells resulted in the stronger backscattered intensity surrounding the damaged vessels and also reduced the backscattered intensity from the damaged vessels. Thus, the estimated SV values of the damaged vessels became much smaller as compared to the result obtained before the MN insertion, causing the broken vascular pattern as shown in Figs. 6(b)-6(e). At 48 hrs after removing the MN patch, the vascular pattern was almost the same as that before the insertion of the patch. Moreover, to further verify the decrease in the SV values of OCT images, the same experimental procedure in Fig. 5 was repeated. Before the insertion of the MN patch, Evans blue dye, used as a contrast agent, was injected into the tail vein before inserting the MN patch. Then, an MN patch was inserted into the mouse ear skin and then, removed after 180 mins. Figures 6(g) and 6(h) show the photos taken before the insertion of the MN patch and after the removal of the MN patch, respectively. Compared with Fig. 6(g), the distribution of blue colour on the mouse ear in Fig. 6(h) can be observed, which resulted from the vessel damage induced by MNs that caused the leakage of Evans blue from the vessels to the surrounding tissue. Here, the use of Evans blue as a contrast agent shows the evidence of blood leakage resulting from the MN insertion, which agrees with the results shown in Fig. 6(b). Therefore, one can see that the MNs can cause vascular damage and that

the damaged vessels can recover in 48 hrs. Moreover, to analyze the change in the SV values, the SV intensities of the grey squares in Figs. 6(a)-6(f) were summarized. Figure 7 shows the summation of SV values as a function of time for regions A, B, C, and D, which are marked by grey squares in Fig. 6(a). For the four different regions, the four curves in Fig. 7 show the same trend. The summation of SV values decreased after the MNs were inserted and then increased over time. By 48 hrs after MN insertion, the summation of the SV values was close to that before the insertion of the MNs for four regions.

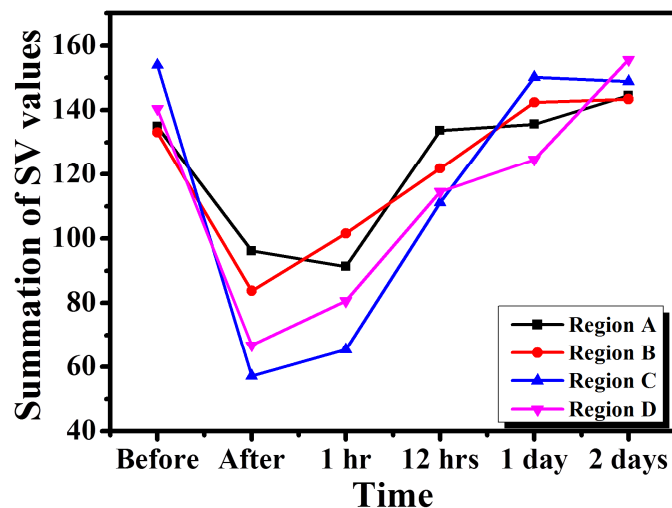


Fig. 7. Summation of SV values of regions A, B, C, and D indicated by the grey squares in Fig. 6 as a function of time.

To implement OCT to observe drug diffusion, rhodamine 6G was used in the experiment exploring the potential for using partially dissolving MNs as a transdermal delivery device. Using the same experimental procedure as shown in Fig. 2, the MN patch was inserted on the ear skin of a mouse and rhodamine 6G was encapsulated in the MNs. After the insertion of the MN patch, sequential B-mode scans at the same location were recorded. Here, to evaluate the variation in the OCT backscattered intensity due to rhodamine diffusion in skin, cross-correlation coefficients between sequential OCT images were estimated. In contrast to the SV estimation, moving particles correspond to low-correlation coefficients between B-mode scans obtained from the same skin location. Therefore, to extract the low-correlation region, a threshold value of 0.15 was set to reject the high-correlation region.

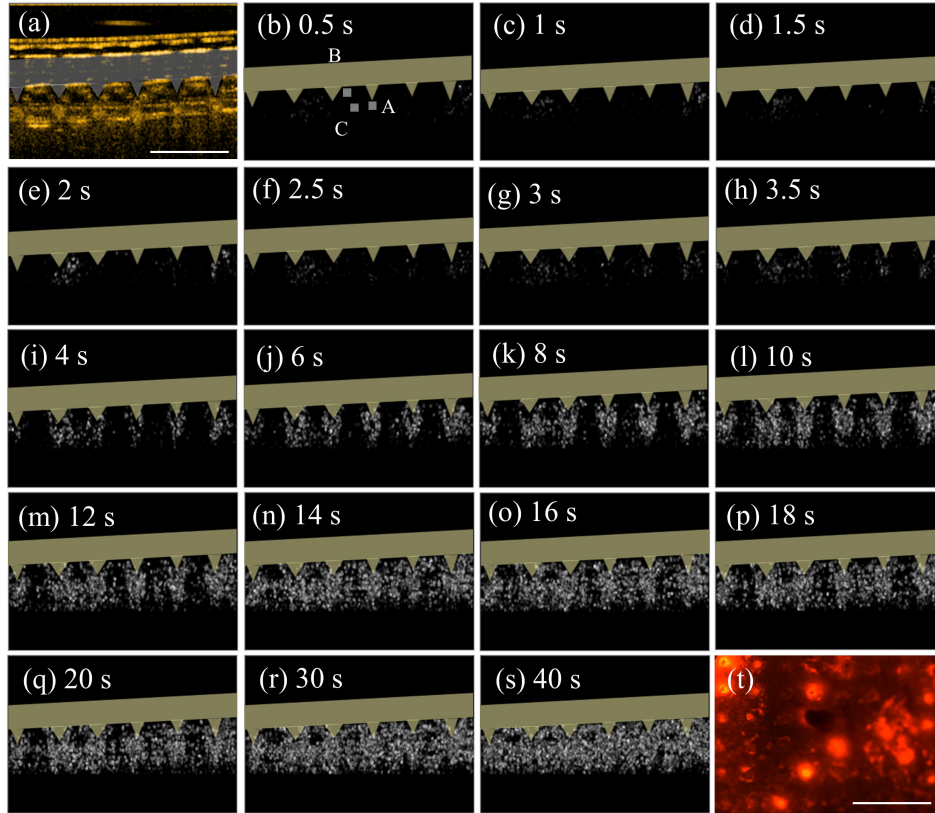


Fig. 8. (a) *In vivo* OCT image after insertion of the MN patch. Time-variant cross-correlation mapping at the same skin location after applying the MN patch to the skin for (b) 0.5 s, (c) 1 s, (d) 1.5 s, (e) 2 s, (f) 2.5 s, (g) 3 s, (h) 3.5 s, (i) 4 s, (j) 6 s, (k) 8 s, (l) 10 s, (m) 12 s, (n) 14 s, (o) 16 s, (p) 18 s, (q) 20 s, (r) 30 s, and (s) 40 s. (f) Fluorescent image after application of the MN patch for 50 s. The brown color in (b)-(s) represents the MN patch structure. The scale bars in (a) and (t) represent 1 mm in length.

To observe the drug diffusion process, the same skin location was repeatedly scanned with OCT during the drug diffusion process and time-series B-mode scans were recorded. Here, we used the B-mode scan obtained when the MN patch was inserted into the skin as a reference image, as shown in Fig. 8(a), and each B-mode scan obtained at the different time points after the insertion of patch was compared to the reference image to acquire the cross-correlation mapping. From Fig. 8(a), the structure of the MN patch and the micro-channels induced by the MNs can be seen. Figures 8(b)-8(s) shows the time-series cross-correlation mapping of the same skin location after inserting the MN patch for (b) 0.5, (c) 1, (d) 1.5, (e) 2, (f) 2.5, (g) 3, (h) 3.5, (i) 4, (j) 6, (k) 8, (l) 10, (m) 12, (n) 14, (o) 16, (p) 18, (q) 20, (r) 30, and (s) 40 s. In Figs. 8(b)-8(s), the low-correlation area gradually increased. From 4 s to 10 s, the distribution of the low-correlation region had an inverted triangle shape, corresponding to the diffusion that occurred at the tip regions of the MNs. After the insertion of the patch for 10 s, low-correlation regions surrounding to the MNs also emerged. By 40 s after the patch insertion, most of the tissue region showed a low-correlation distribution. After the insertion of the MN patch for 50 s, the MN patch was removed from the skin and examined by fluorescence microscopy. Figure 8(t) represents the fluorescent image obtained after removing the patch from the skin, showing the red-colour distribution resulting from rhodamine diffusion into the surrounding skin tissue. To further understand the increase in the area of low-correlation coefficients, three different regions were selected, as indicated by the grey squares in Fig. 8(a). Figure 9 illustrates the total areas of low correlation in regions A, B, and C as a function

of time. For regions A, B, and C, the areas of low correlation started to increase after insertion of the MNs for 4 s; all three regions reached an approximately saturated level after 20 s. Here, region A is located at the tip region of the MN, and regions B and C correspond to the surrounding regions of the MN.

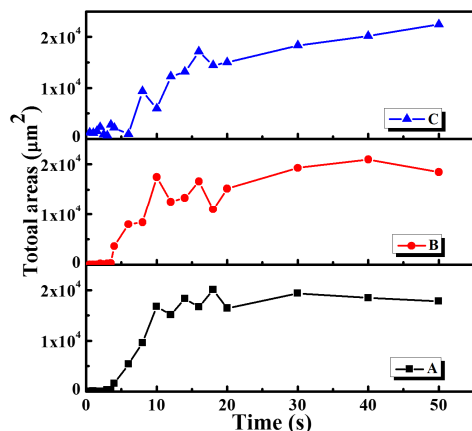


Fig. 9. Total areas of low correlation in regions A, B, and C indicated by the grey squares in Fig. 8 as a function of time.

#### 4. Discussion

In this study, the temporal effects on skin when using MNs for transdermal drug delivery are investigated. With 2D/3D OCT scanning, the dissolution process of a MN in skin can be observed *in vivo* and quantitatively evaluated. *En-face* images extracted from 3D imaging enable the time-dependent changes in the area around the MN at the various skin depths to be identified. From the results shown in Fig. 4, it can be observed that the areas of the induced micro-channels decrease as the depth increases, in accordance with the needle shape. Moreover, the ratios of the mean area at 180 mins to the mean area at 0 mins at the depths of 100, 200, and 300 μm are 26.9%, 13.9%, and 13.6%, respectively, illustrating that the dissolving velocity at the deeper depth is greater than that at the shallow depth. Aside from the observation of MN dissolution in skin with OCT, the skin recovery after MN implementation is also investigated. The results show that skin indentations induced by the MNs can recover in 48 hrs. In addition, MNs may cause damage to vessels, causing blood leakage from the vessels to the surrounding tissue. The OCT results also show that the damage to the vessels can recover in 48 hrs. However, the broken vessels induced by MNs may improve the treatment outcomes by promoting faster drug administration through blood circulation. Finally, a method is also proposed to investigate the drug diffusion through MNs into the surrounding tissue, based on the evaluation of cross-correlation relationship between sequential OCT images obtained at the same locations. Although the dissolution of the used MNs can be observed within 180 mins, drug diffusion from the MNs to the tissue occurred in ten seconds, which can be seen in Fig. 8. This information indicates that MNs used as a TDDS can effectively improve drug delivery in the skin.

#### Acknowledgment

The authors acknowledge financial support in partial from the Ministry of Science and Technology of the Republic of China (ROC), Taiwan (MOST 104-2221-E-182-027-MY2 and 104-2221-E-182-023-MY2) and Chang Gung Memorial Hospital, Taiwan (CMRPD2B0033, CIRPD2E0041, and CMRPD2C0043).